



# Modeling and simulation of heat transfer, fluid flow and geometry morphology in GMAW-based wire arc additive manufacturing

Wenyong Zhao<sup>1</sup> · Yanhong Wei<sup>1</sup> · Jinwei Long<sup>1</sup> · Jicheng Chen<sup>2</sup> · Renpei Liu<sup>1</sup> · Wenmin Ou<sup>3</sup>

Received: 2 February 2021 / Accepted: 2 April 2021 / Published online: 15 April 2021  
© International Institute of Welding 2021

## Abstract

In this study, we develop a 3D transient mathematic model to simulate the heat transfer, fluid flow, and geometry morphology in GMAW-based wire arc additive manufacturing (WAAM). The processes of droplet formation, growth, and detachment from the end of wire electrode, who travels dynamically along the scanning direction, are coupled with molten pool for the first time by considering their own mechanical conditions and solving the transport equations in the whole solution domain. By the developed model, the simulations of single-pass multi-layer of WAAM of Al-5%Mg are performed. The calculated results indicate that when the droplet falls into the molten pool, the maximum velocity inside the droplet reaches 0.9m/s, resulting in that liquid metal in the middle flows toward the bottom of the molten pool and a depressed region is formed. On the surface of molten pool, the liquid metal dominated by Marangoni force flows from center to periphery, and on the bottom of molten pool, a clockwise circulation is formed. In addition, the interlayer idle time contributes to the formation of deposit with higher height and narrow width. Finally, to validate the model, the deposit profiles are also compared between simulated and experimental results.

**Keywords** Wire arc additive manufacturing · Droplet transfer · Molten pool · Coupled model · Single pass multi layers

Recommended for publication by Commission I - Additive Manufacturing, Surfacing, and Thermal Cutting

## Highlights

1. A three-dimensional mathematic model is developed to simulate the heat and metal transfer and fluid flow in GMAW-based wire arc additive manufacturing.
2. The droplet formation, growth, and detachment at the end of wire electrode moving dynamically along the scanning direction are coupled to the molten pool for the first time.
3. The droplet falls into the molten pool with a maximum velocity of 0.9m/s inside, resulting in an expansion of molten pool size and a depressed region formed in the molten pool.
4. The metal collapse occurs at the ends of deposition layer in single-pass multi-layer WAAM, resulting in an increase in the length of deposit.
5. The simulated results are in a good agreement with experimental measurements in the deposit profiles.

✉ Yanhong Wei  
nuaadw@126.com

✉ Wenmin Ou  
ouwenmin@cslg.edu.cn

<sup>1</sup> College of Material Science and Technology, Nanjing University of Aeronautics and Astronautics, Nanjing 210016, China

<sup>2</sup> MIIT Key Laboratory of Pattern Analysis and Machine Intelligence, College of Computer Science and Technology, Nanjing University of Aeronautics and Astronautics, Nanjing 210016, China

<sup>3</sup> School of Automotive Engineering, Changshu Institute of Technology, Changshu 215500, China

## 1 Introduction

Metal additive manufacturing (MAW), a revolutionary advanced manufacturing technology, has attracted significant academic and industry interest in recent years owing to its ability to directly fabricate various complex or customized parts with low material wastage, short leading time, and customizable material properties [1]. As the most representative method of MAW, wire arc additive manufacturing (WAAM) developed from gas metal arc welding (GMAW), gas tungsten arc welding (GTAM), or plasma arc welding (PAW) is regarded as the most suitable candidate to fabricate large-scale metallic structure for the high deposition rates and low feedstock and equipment costs [2, 3]. Generally, WAAM process involves multiple complicated physical phenomena, including the melting of filler wire, the transition of droplets, the convective flow of high-temperature liquid metal inside the molten pool, the deformation of molten pool free surface, and the solidification of liquid metal [4, 5]. These complex physical processes comprehensively determine the shape and size of deposited layers [6], the microstructure [7], mechanical properties [8, 9], residual stresses, and distortion of components [10]. Therefore, creating a high surface finish, defect-free, and excellent mechanical component requires the

accurate control of process parameters such as welding current, voltage, wire feed rate, travel speed, shielding gas type and flux, and the waiting time between layers, which significantly affect the above physical phenomena. Trial-and-error methodology is the conventional and currently the majority approach to study such problems. A. Gomez Ortega [11] reported the effect of process parameters on the geometrical characteristics of monolayer and multi-layer deposition of Al5Si alloy by WAAM. It was found that a gradual increase of travel speed was required to keep a constant layer width for the fabrication of multi-layer walls, which resulted from the heat accumulation of layer-by-layer stacking. In order to improve the geometry precision of parts, Xiong [12] used visual inspection of previous and current layers to achieve the excellent control of deposition height in WAAM via controlling the wire feed speed. The inter-pass cooling conditions have a significant influence on the morphology, microstructure, and mechanical properties of parts, as reported by [13]. Uwe Reisgen [14] proposed different process cooling strategies to increase the manufacturing efficiency of WAAM and pointed out that aerosol cooling can be a promising addition. M.J. Bermingham [15] explored additional post-processes such as heat treatment to optimize the mechanical properties of TC4 components fabricated by WAAM and found that stress relief treatments can improve the ductility by over 30%. Cong [16] systematically investigated the influence of arc mode in cold metal transfer (CMT) process, an advanced GMAW, on the porosity of additively manufactured Al-6.3Cu alloy. It was concluded that CMT pulse advanced was the most suitable process to deposit the aluminum alloy for the advantage of low heat input, and with the appropriate parameters, gas pores can be eliminated. However, this traditional experimental method is time-consuming, laborious, and expensive, especially for precious or rare metals. It is not only difficult to quantitatively analyze the internal physical mechanism but against the new development concepts of intelligent manufacturing and green manufacturing.

Numerical simulation, a powerful investigation method, provides an alternate solution to overcome the shortcomings of trial-and-error method. By discretizing and solving the corresponding governing equations, numerical simulation can visualize the evolution of various physical fields with scales ranging from macroscopic mechanical properties to microstructure morphology, so it conveniently assists to understand the internal physical mechanism in WAAM and guides the process optimization. Although GMAW-based WAAM is derived from GMAW which can be referenced, many existed mathematic models of GMAW are static welding and not suitable to apply to WAAM directly. Zhou [17] developed a 3D weak coupled arc and metal transport model and successfully simulated the arc, molten pool dynamic, and impingement of droplet in GMAW-based WAAM. By simplifying the molten pool to be solid state, the arc was calculated firstly to

obtain the electromagnetic force, arc pressure, plasma shear stress, and heat flux, which were then transmitted to metal transport model as input. However, in metal transport model, the droplet was assumed to be a constant sphere and generated at a certain frequency, which was inconsistent with the process of droplet formation, growth, detachment, and entry into the molten pool in WAAM. Bai [18] developed a 3D model to analyze the fluid flow and heat transfer behaviors in multi-layer deposition of PAW-based WAAM. The volume of fluid (VOF) method was used to track the free surface of molten pool, and the porosity enthalpy method was employed to track the solid-liquid interface. Similar to the Zhou's [17] model, the droplet transfer process was modeled as a mass source term in continuity equation, and the mass input position was a spherical region, which was determined by the actual experimental data. Y. Ogino et al. [19] proposed a 3D simplified model to simulate the WAAM process; the effect of deposition condition including inter-pass temperature, welding direction, and procedure on the shape of deposit was investigated, while the formation, growth, and detachment of droplet were also neglected. Hejrjipour [20] proposed a finite element model (FEM) to predict the first layer profile of WAAM process with dissimilar substrate. In this model, the current density, heat input, and arc pressure were considered as Gaussian distribution, and the profile of molten pool was computed from the minimization of the total potential energy of surface instead of VOF. To validate the simulation results, experiments were performed which showed a good agreement. Nevertheless, this model is hard to apply for multi-layer deposition, and the selections of arc efficiency, arc radius, and arc pressure require multiple computations by comparing numerical and experimental profiles of the weld pool. In order to omit the tedious verification and accurately describe the actual physical phenomena of droplet detachment, transfer into the molten pool and molten pool dynamic. Cadieux [21] developed a 2D axisymmetric multi-physics model, considering the electromagnetism, fluid flow, and heat transfer in the droplet and molten pool. In this model, level set method was used in tracking interface, and operating parameters were the only knowledge that is required to simulate the geometry of component as well as its temperature field and velocity field without any assumption. However, because of the inherent shortcomings of 2D model, this model is only able to simulate one cross section of component similar to spot welding and can't show 3D complete geometric features and the distribution of field variables at the third direction. What is needed but not currently available is a three-dimensional integrated multi-physics process model of WAAM that can accurately predict the evolution of morphology and various physical field variables under different process parameters, and such model will be of great value in forming control and the prediction of microstructure and mechanical properties.

In this paper, we develop a three-dimensional transient heat transfer and fluid flow model of GMAW-based WAAM, where the processes of droplet formation, growth, and detachment from the end of wire electrode, who travels dynamically along the scanning direction, are coupled with molten pool for the first time by considering their own mechanical conditions and solving the transport equations in the whole solution domain. The enthalpy-porosity method is used to handle the metal melting and solidification, and the dynamic meshing technique is used to extend the solution domain. This 3D model has the ability to reproduce the impingement of droplet into molten pool, the deformation of free surface of molten pool, and the molten metal collapse during multi-layer WAAM. It can also predict the influence of interlayer cooling condition on the deposit profile.

## 2 Experimental procedure

In this investigation, the wire of ER5356 with 1.2-mm diameter is used to fabricate a series of 40-mm-long deposited layers on a 50 mm×30 mm×4 mm baseplate of 5A05. The nominal chemical compositions of 5A05 and ER5356 are listed in Table 1. The schematic of WAAM system is shown in Fig. 1, a Panasonic digital MIG/MAG welding power source of direct current is used as heat source, and a six-axis-independent welding robot with control box and wire feed system is employed to achieve the motion of torch. The shielding gas is high-purity argon (99.99%). According the preliminary process window exploration, the process parameters, listed in Table 2, are used for the manufacturing of the single-pass single layer (SPSL), single-pass two layers (SPTL), and single-pass five layers (SPFL). The final products are shown in Fig. 2. In order to study the effects of idle time, two different cases of SPTL are considered. Figure 2b shows the deposit without interlayer idle time. Figure 2c shows the deposit with enough interlayer idle time to cool the temperature to 300K which is measured by handheld infrared thermometer. For the deposition of SPFL, it is conducted with enough interlayer idle time same as SPTL, shown in Fig. 2d. After the deposition, the middle cross sections of deposited beads are obtained by electric spark cutting, grinding, polishing, and etching using 20% hydrofluoric acid (HF) for 30s.

**Table 1** The nominal chemical composition of used alloys (wt%)

Material	Si	Fe	Cu	Mn	Mg	Cr	Zn	Ti	Al
5A05	0.5	0.5	0.1	0.3–0.6	4.8–5.5	/	0.2	0.06–0.2	Bal.
ER5356	0.25	0.4	0.1	0.05–0.2	4.5–5.5	0.05–0.2	0.2	/	Bal.

## 3 Mathematical models

A three-dimensional transient numerical model is developed to investigate the heat transfer, metal transfer, and fluid flow of GMAW-based WAAM with droplet and molten pool coupled. The solution domain consists of air subdomain and metal subdomain, as shown in Fig. 3. Due to the geometric symmetry with respect to XZ plane, half of solution domain is used. The metal subdomain is the substrate whose size is 50 mm × 15 mm × 5mm. The air subdomain contains the shielding gas, droplet, molten pool, and solidified metal deposited layer by layer. The dynamic meshing technique is employed to expand the air subdomain along the deposition direction, whose initial height is set as 7mm according to the experimental observation of the location where wire begins to melt. The bidirectional scanning direction is adopted for multi-layers along the X axis. The areas of shielding gas inlet and liquid metal inlet are at the end of torch. The height of air subdomain increases by the same distance as the welding torch lift for each deposited layer, and this distance,  $H_l$ , can be obtained by Eq. (1) [22].

$$H_l = \frac{A_{cs1}}{W_b} \quad (1)$$

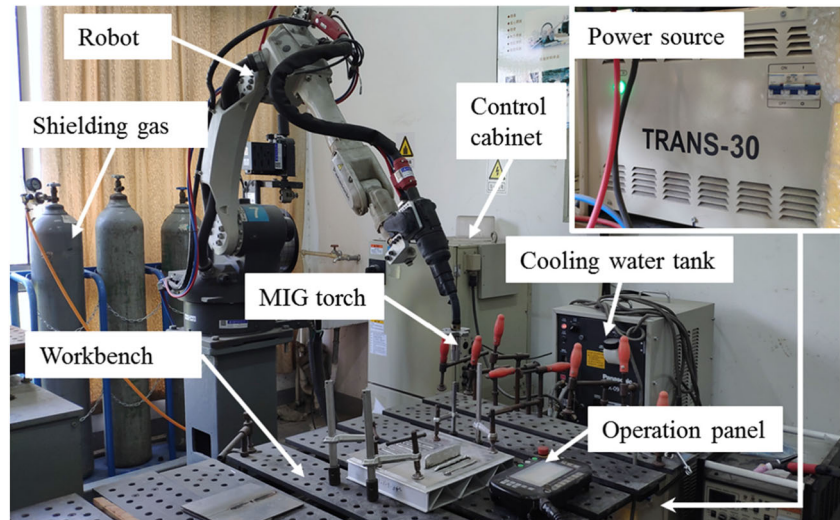
where  $A_{cs1}$  and  $W_b$  are the cross-sectional area and the width of the first deposited layer, respectively.

### 3.1 Assumptions

Due to the complexity of the actual physical phenomena of WAAM and the rapid increase of calculation time, it is not realistic to couple all physical processes into a model for numerical simulation. Therefore, the following simplified assumptions are made to reduce the difficulty of modeling:

- (1) The process of wire feeding is equivalent to high-temperature liquid metal flowing from a virtual tube, and the velocity of liquid metal is equal to the wire feed rate [23].
- (2) Because the computational domain is expanding as the deposition layer increases, the shielding gas inlet is assumed to be at the same height as the liquid metal, and the mixture of shielding gas and air above the substrate is regard as pure argon.

**Fig. 1** The wire arc additive manufacturing system



- (3) The liquid metal is considered to be a laminar, incompressible, and Newtonian fluid [24], and the heat and mass loss caused by vaporization of liquid is not considered.
- (4) The thermal buoyancy-driven flow is calculated by Boussinesq approximation.
- (5) The arc plasma is neglected in the current model to furtherly save the simulation time, and the heat transfer to liquid metal is considered by a volumetric heat source.

### 3.2 Governing equations

Base on the abovementioned assumptions, the following partial differential equations governing the conservation equations of mass, momentum, and energy are solved:

Mass conservation equation:

$$\nabla \cdot (\rho \vec{V}) = 0 \quad (2)$$

Momentum conservation equation:

$$\frac{\partial \rho \vec{V}}{\partial t} + \nabla \cdot (\rho \vec{V} \vec{V}) = \nabla \cdot (\mu \nabla \vec{V}) - \nabla p + \vec{F}_{\text{Darcy}} + \vec{F}_{\text{liquid}} \quad (3)$$

**Table 2** Deposition parameters used in experiments and simulations

Deposition parameters	Unit	Value
Deposition current	A	135
Deposition voltage	V	16
Travel speed	cm/min	120
Wire feeding speed	cm/min	900
Wire diameter	mm	1.2
Shielding gas flow rate	L/min	20

Energy conservation equation:

$$\frac{\partial(\rho H)}{\partial t} + \nabla \cdot (\rho \vec{V} H) = \nabla \cdot (k \nabla T) + q_{\text{arc}} + q_{\text{loss}} \quad (4)$$

where  $\rho$  is density,  $\vec{V}$  is velocity vector,  $\mu$  is viscosity,  $p$  is pressure,  $\vec{F}_{\text{Darcy}}$  is the momentum sink of partially solidified region,  $\vec{F}_{\text{liquid}}$  is the total momentum source of liquid metal region resulting from various surface force and volume force,  $H$  is the enthalpy,  $k$  is thermal conductivity,  $T$  is temperature,  $q_{\text{arc}}$  is the arc heat, and  $q_{\text{loss}}$  is the heat loss.

The VOF technique, reported by Torrey [25], is adopted to track the metal-gas interface, and its equation can be written as:

$$\frac{\partial F}{\partial t} + \nabla \cdot (\vec{V} F) = 0 \quad (5)$$

where the scalar function  $F$  denotes the volume fraction of fluid. For two-phase flow model of metal liquid and argon liquid, the case of  $F=1$  represents cells are full of liquid metal, the case of  $F=0$  represents cells are full of argon, and the case of  $0 < F < 1$  represents the cells contain the interface between liquid metal and argon. In the VOF model, the material properties appearing in the transport equations are determined by the presence of the component phases in each control volume, such as the density in the two-phase flow model, which is calculated by:

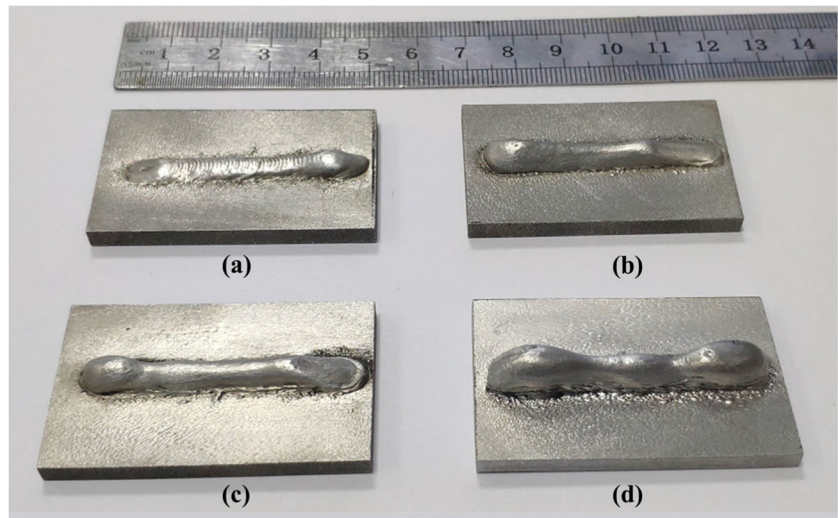
$$\rho = F \rho_{\text{metal}} + (1-F) \rho_{\text{gas}} \quad (6)$$

where  $\rho_{\text{metal}}$  is the density of metal phase and  $\rho_{\text{gas}}$  is the density of the gas phase.

The enthalpy-porosity technique [26] is employed to track the liquid-solid interface, which treats the mushy zone as a porous medium. The porosity is equal to the liquid fraction



**Fig. 2** The fabricated products using the process parameters listed in Table 2: **a** SPSL; **b** SPTL without interlayer idle time; **c** SPTL with enough interlayer idle time until 300K; **d** SPFL with enough interlayer idle time until 300K



in each cell. The momentum sink caused by decreased porosity in mushy region is added to the momentum equation as a source term:

$$\vec{F}_{\text{Darcy}} = \frac{(1-f_l)^2}{(f_l^3 + \varepsilon)} A_{\text{Darcy}} \vec{V} \tag{7}$$

where  $\varepsilon$  is a small number (0.001) to prevent division by 0,  $A_{\text{Darcy}}$  is mushy zone constant, and the higher this value, the faster of the velocity of material to zero as it solidifies. Since excessively large values may lead the solution to oscillate, values between  $10^4$  and  $10^7$  are commonly recommended for many calculations.  $f_l$  is liquid volume fraction and is assumed to vary linearly with temperature:

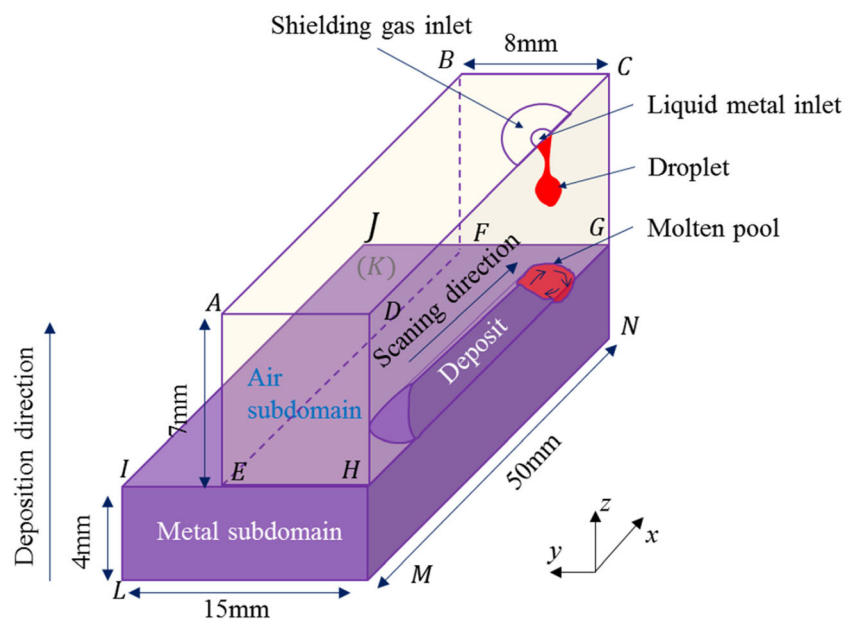
$$f_l = \begin{cases} 0 & \text{if } T < T_s \\ \frac{T-T_s}{T_1-T_s} & \text{if } T_s \leq T \leq T_1 \\ 1 & \text{if } T > T_1 \end{cases} \tag{8}$$

The governing equations are solved in the whole domain, but the mechanical source terms  $F_{\text{liquid}}$  of momentum between droplet model and molten pool model are slightly different in Sects. 3.3 and 3.4.

### 3.3 Droplet mechanical model

In GMAW process, the welding wire acts as an electrode, and its tip melts to form droplets. During the droplet formation,

**Fig. 3** Schematic of solution domain



evolution, and detachment, the forces acting on droplets involve gravity  $\vec{F}_g$ , buoyancy force  $\vec{F}_{\text{buo}}$ , surface tension  $\vec{F}_{\text{st}}$ , Marangoni force  $\vec{F}_{\text{Ma}}$ , electromagnetic force  $\vec{F}_{\text{emd}}$ , and plasma drag force  $\vec{F}_{\text{pd}}$  [27]. Hence, the  $F_{\text{liquid}}$  of droplet model satisfies:

$$\vec{F}_{\text{liquid}} = \vec{F}_g + \vec{F}_{\text{buo}} + \vec{F}_{\text{st}} + \vec{F}_{\text{Ma}} + \vec{F}_{\text{emd}} + \vec{F}_{\text{pd}} \quad (9)$$

The momentum source term for gravity is expressed as Eq. (10), and the buoyancy force caused by the difference of liquid metal density is considered by Boussinesq approximation and is written as Eq. (11):

$$\vec{F}_g = \rho_{\text{metal}} \vec{g} \quad (10)$$

$$\vec{F}_{\text{buo}} = -\rho \vec{g} \beta (T - T_l) \quad (11)$$

where  $\vec{g}$  is acceleration of gravity,  $\beta$  is thermal expansion coefficient, and  $T_l$  is liquidus temperature.

Surface tension is a force on the free surface of droplet and molten pool, which arises as a result of attractive force between molecules in a fluid, and can be described as the product of surface tension coefficient  $\gamma$  and interface curvature  $\kappa$ :

$$\tau_{\text{st}} = \gamma \kappa \quad (12)$$

Due to the moving of heat source, the distribution of temperature on the liquid metal surface is non-uniform, and a spatial gradient of surface tension, that is, Marangoni force, will be generated, which promotes the convection of liquid metal in the molten pool:

$$\tau_{\text{Ma}} = \frac{\partial \gamma}{\partial T} \frac{\partial T}{\partial \vec{s}} \quad (13)$$

where  $\vec{s}$  is the vector to free surface.

Because the metal-gas interface is an implicit interface which is tracked by the fluid volume between 0 and 1, the surface forces cannot be applied directly. Continuum surface force (CSF) method [28] is usually adopted to convert the surface force to volume force by multiplying a volume fraction gradient term. Therefore, volumetric form of surface tension and Marangoni force can be expressed as:

$$\vec{F}_{\text{st}} = \tau_{\text{st}} \nabla F \frac{2\rho}{\rho_{\text{metal}} + \rho_{\text{gas}}} \quad (14)$$

$$\vec{F}_{\text{Ma}} = \tau_{\text{Ma}} \nabla F \frac{2\rho}{\rho_{\text{metal}} + \rho_{\text{gas}}} \quad (15)$$

The electromagnetic force is the result of the interaction of the current flowing the droplet and its own induced magnetic field. Generally, the distribution of current density in the droplet is difficult to obtain by the experimental measurements. In this study, we adopt the hypothesis proposed in Ref. [27],

which considers that the current density is uniformly distributed at the interface between the droplet and wire and Gauss distributed at the end of droplet. Hence, the component of electromagnetic force along x, y, and z directions can be expressed as follows:

$$B_d = \frac{\mu_0 I r (1 - z/H_0)}{4\pi R_w^2} + \frac{\mu_0 I z}{4\pi H_0 r} (1 - \exp(-k_d r^2)) \quad (16)$$

$$\vec{F}_{\text{emdx}} = B_d \left( \frac{rI}{4\pi R_w^2 H_0} - \frac{k_d I r \exp(-k_d r^2)}{4\pi H_0} \right) * \frac{x}{r} \quad (17)$$

$$\vec{F}_{\text{emdy}} = B_d \left( \frac{rI}{4\pi R_w^2 H_0} - \frac{k_d I r \exp(-k_d r^2)}{4\pi H_0} \right) * \frac{y}{r} \quad (18)$$

$$\vec{F}_{\text{emdz}} = B_d \left( \frac{I \left(1 - \frac{z}{H_0}\right)}{2\pi R_w^2} + \frac{k_d I z \exp(-k_d r^2)}{2\pi H_0} \right) \quad (19)$$

where  $B_d$  is induced magnetic field intensity,  $r$  is the radial distance from the end of wire,  $I$  is current,  $R_w$  is wire radius,  $H_0$  is the length of droplet,  $k_d$  is current concentration factor determined by  $\frac{1}{\sigma_j^2}$ ,  $\sigma_j$  is the distribution radius of current, and  $\mu_0$  is magnetic permeability.

The plasma drag force on the droplet can be regarded as the pulling force on the sphere immersed in the moving fluid. In a fluid with uniform velocity, the pulling force on a sphere can be expressed as [29]:

$$\vec{F}_{\text{pd}} = C_d A_p \rho_f v_f^2 / (2 * \rho V_D) \quad (20)$$

where  $C_d$  is plasma flow coefficient,  $A_p$  is acting area of plasma determined by  $\pi(R_d^2 - R_w^2)$ , the  $R_d$  is the droplet equivalent radius, the  $R_w$  is radius of droplet necking position, the  $\rho_f$  is the density of plasma,  $v_f$  is the velocity of plasma, and  $V_D$  is droplet volume. In this study, the value of  $\rho_f$  is approximated to argon density ( $6e^{-6} \text{kg/m}^3$ ), and  $v_f$  is assumed to be 100m/s.

### 3.4 Molten pool mechanical model

The fluid flow of molten pool has an important influence on the final geometry of deposited layer. In the present model, the body forces including gravity, buoyancy force, and electromagnetic force and the surface forces including surface tension, Marangoni force, and arc pressure are considered in the molten pool. The impact of droplet on molten pool is reflected automatically by solving the mass and momentum conservation equations uniformly in the whole solution domain. Therefore, the source term of momentum,  $F_{\text{liquid}}$  for molten pool model can be written as:

$$\vec{F}_{\text{liquid}} = \vec{F}_g + \vec{F}_{\text{buo}} + \vec{F}_{\text{em}} + \vec{F}_{\text{st}} + \vec{F}_{\text{Ma}} + \vec{F}_{\text{arc}} \quad (21)$$

where the gravity, buoyancy force, surface tension, and

Marangoni force of liquid metal in molten pool are the same as that of droplet model and can be obtained by Eqs. (10), (11), (12), (13), (14), and (15).

Similar to the droplet model, there is an induced magnetic field in the molten pool. Assuming that the current density is also Gauss distributed in molten pool [30], the electromagnetic force in the molten pool can be expressed as:

$$\vec{F}_{emmx} = \frac{\mu_0 I^2 x}{4\pi^2 r^3 L} \left[ 1 - \exp\left(-\frac{r^2}{\sigma_j^2}\right) \right]^2 \left(1 - \frac{z-z_0}{L}\right) \quad (22)$$

$$\vec{F}_{emmy} = \frac{\mu_0 I^2 y}{4\pi^2 r^3 L} \left[ 1 - \exp\left(-\frac{r^2}{\sigma_j^2}\right) \right]^2 \left(1 - \frac{z-z_0}{L}\right) \quad (23)$$

$$\vec{F}_{em mz} = \frac{\mu_0 I^2}{2\pi^2 r \sigma_j^2} \exp\left(-\frac{r^2}{\sigma_j^2}\right) \left[ 1 - \exp\left(-\frac{r^2}{\sigma_j^2}\right) \right] \left(1 - \frac{z-z_0}{L}\right)^2 \quad (24)$$

where  $L$  is the thickness of substrate and  $z_0$  is z-coordinate value of arc starting location.

The arc pressure is the total pressure of arc plasma falling on the surface of the substrate and affected by current density of deposition [31]:

$$P_{arc} = \frac{\mu_0 I^2}{8\pi\sigma_p^2} \exp\left(-\frac{r^2}{2\sigma_p^2}\right) \quad (25)$$

where  $\sigma_p$  is distribution radius of arc pressure. Arc pressure is reformulated as body force terms by using the CSF method as follows:

$$\vec{F}_{arc} = P_{arc} \nabla F \frac{2\rho}{\rho_{metal} + \rho_{gas}} \quad (26)$$

### 3.5 Heat source model

In GMAW process, the heat of welding arc is not only used to heat the base metal to generate molten pool but also used to heat the wire to form molten droplets. In the current model, the liquid metal is assumed to flow from the wire tip at a constant temperature of 1506K to form droplet, and during the growth and detachment of droplet, heat convection and heat radiation are experienced, as described in Sect. 3.6. The welding arc moves along the scanning direction, and the distribution of arc heat flux density is no longer a uniform circle, but a double ellipsoid with a wide back and a narrow front. Therefore, the Goldak’s double ellipsoidal heat source model is more favored and employed in current model to achieve the direct heating of the welding arc. The computing heat flux is added to energy equation as a source term:

$$q_{arc} = \begin{cases} \frac{6\sqrt{3}f_f \eta UI}{a_f b c \pi \sqrt{\pi}} \exp\left(-3\left(\frac{(x-x_0-V_T t)^2}{a_f^2} + \frac{(y-y_0)^2}{b^2} + \frac{(z-z_0)^2}{c^2}\right)\right) & ((x-x_0-V_T t) > 0) \\ \frac{6\sqrt{3}f_r \eta UI}{a_r b c \pi \sqrt{\pi}} \exp\left(-3\left(\frac{(x-x_0-V_T t)^2}{a_r^2} + \frac{(y-y_0)^2}{b^2} + \frac{(z-z_0)^2}{c^2}\right)\right) & ((x-x_0-V_T t) < 0) \end{cases} \quad (27)$$

The heat source model is established in the workpiece coordinate system, where the location  $(x_0, y_0, z_0)$  is the starting point of each layer deposition and the location  $(x_0 + V_T t, y_0, z_0)$  is the current point of arc bottom center.  $U$  is voltage, and  $\eta$  is the arc efficiency for heating molten pool, excluding heating droplets, which is described in detail in Ref. [32].  $f_f$  and  $f_r$  are the heat distribution coefficients of the front and rear semi-ellipsoids, and the sum of two is equal to 2. The geometric dimensions of heat source,  $a_f$ ,  $a_r$ ,  $b$ , and  $c$  are obtained by comparing the calculated and experimental morphologies of molten pool of first deposition layer, which are 3mm, 6mm, 4mm, and 4mm, respectively, under the deposition parameters shown in Table. 2.

### 3.6 Boundary conditions

Table 3 shows the boundary conditions used in this study, corresponding to Fig. 3. The top surface  $ABCD$  of air

subdomain is velocity inlet boundary, including the shielding gas and liquid metal. Liquid metal inlet is an area where filler wire is located and travels over time. The shielding gas inlet is a region where nozzle is located except wire, and its maximum radius is 10mm in this study. The inlet velocity of liquid metal is equal to wire feeding speed that of shielding gas is calculated by Eq. (28) [21], and that of other region of inlet boundary is zero.

$$V_{gas}(r) = \frac{2Q_v}{\pi} \frac{\left[ R_{nozzle}^2 - r^2 + (R_{nozzle}^2 - R_w^2) \frac{\ln(r/R_{nozzle})}{\ln(R_{nozzle}/R_w)} \right]}{\left[ R_{nozzle}^4 - R_w^4 + \frac{(R_{nozzle}^2 - R_w^2)^2}{\ln(R_{nozzle}/R_w)} \right]} \quad (28)$$

where  $Q_v$  is volume flow rate of shielding gas and  $R_{nozzle}$  is the internal radius of nozzle.

Heat loss from convection and radiation occurs not only on the wall boundaries but also on the free surface of molten pool

**Table 3** Boundary conditions

Boundary		$T$	$\vec{V}$	$p$	$F$
ABCD (velocity inlet)	If $r < R_w$	$T=1506\text{K}$	$V_z=0.15\text{m/s}$	Atmosphere pressure	1
	If $R_w < r < R_{\text{nozzle}}$	$T=300\text{K}$	$V_z = -V_{\text{gas}}$		0
	If $r > R_{\text{nozzle}}$	$T=300\text{K}$	$V_z=0$		0
AEFB, ADHE, BCGF (pressure outlet)		$T=300\text{K}$	—	Atmosphere pressure	—
CDHG, HGNM (symmetry)		$\frac{\partial T}{\partial n} = 0$	$\frac{\partial V}{\partial n} = 0, V_y=0$	—	—
EFJI, IJKL, IHML, JGNK (wall)		Eq. (29)	$\vec{V}=0$	—	—

and droplets. It should be noted that corresponding heat loss of free surface needs to be reformulated as volumetric heat source by CSF.

$$q_{\text{loss}} = -(h(T - T_a) + \varepsilon_b \sigma_b (T^4 - T_a^4)) |\nabla F| \frac{2\rho}{\rho_{\text{metal}} + \rho_{\text{gas}}} \quad (29)$$

where  $h$  is heat transfer coefficient,  $T_a$  is ambient temperature,  $\varepsilon_b$  is emissivity, and  $\sigma_b$  is Stefan-Boltzmann constant.

Due to similar chemical compositions, the thermo-physical properties of substrate and wire used in simulation are assumed to be consistent and isotropic. The thermo-physical properties of 5A05 and other physical variables are listed in Table 4, and for partial parameters not available, they are estimated from pure aluminum or aluminum alloys with similar compositions.

**Table 4** Thermo-physical properties of 5A05 and other parameters used in simulation

Properties and parameters (unit)	Value
Density ( $\text{kg} \cdot \text{m}^{-3}$ )	2650
Solidus temperature (K)	815 [33]
Liquidus temperature (K)	906 [33]
Specific heat ( $\text{J} \cdot \text{kg}^{-1} \cdot \text{K}^{-1}$ )	Temperature-dependent [33]
Thermal conductivity ( $\text{W} \cdot \text{m}^{-1} \cdot \text{K}^{-1}$ )	Temperature-dependent [33]
Viscosity ( $\text{kg} \cdot \text{m}^{-1} \cdot \text{s}^{-1}$ )	Temperature-dependent [33]
Surface tension coefficient ( $\text{N} \cdot \text{m}^{-1}$ )	0.85 [34]
Temperature coefficient of surface tension ( $\text{N} \cdot \text{m}^{-1} \cdot \text{K}^{-1}$ )	$-1.55 \times 10^{-4}$ [34]
Latent heat of melting ( $\text{J} \cdot \text{kg}^{-1}$ )	$3.58 \times 10^5$ [33]
Thermal expansion coefficient ( $\text{K}^{-1}$ )	$3 \times 10^{-5}$ [33]
Heat transfer coefficient ( $\text{W} \cdot \text{m}^{-2} \cdot \text{K}^{-1}$ )	80
Magnetic permeability ( $\text{H} \cdot \text{m}^{-1}$ )	$4\pi \times 10^{-7}$
Stefan-Boltzmann constant ( $\text{W} \cdot \text{m}^{-1} \cdot \text{K}^{-1}$ )	$5.67 \times 10^{-8}$
Acceleration of gravity ( $\text{m} \cdot \text{s}^{-2}$ )	9.81
Atmosphere pressure ( $\text{N} \cdot \text{m}^{-2}$ )	101,300
Arc efficiency	0.7 [29]
Plasma flow coefficient	0.44 [27]
Distribution radius of current (m)	0.002 [estimated]
Distribution radius of arc pressure (m)	0.002 [estimated]

### 3.7 Solution method

The whole solution domain is divided into regular hexahedral control cells, and the initial number of cells is 256512, whose minimum size is 0.25 mm. Starting from the 2nd layer, the number of cells increases by 26720 for each deposited layer. Governing equations are discretized by the finite volume method, and the velocity-pressure coupling is solved by pressure implicit with splitting of operators (PISO) algorithm. The calculations are completed using a commercial CFD solver Fluent extended with self-coded subroutines, with a time step of  $4 \times 10^{-5}$  s. For the computation of single deposited bead with the length of 40mm, it takes approximately 100 h to simulate the 2 s of real-time deposition in the case of 16-core parallel, which is performed on a computer with 2.3-GHz Xeon-E5 CPU and 128-GB RAM.

## 4 Results and discussions

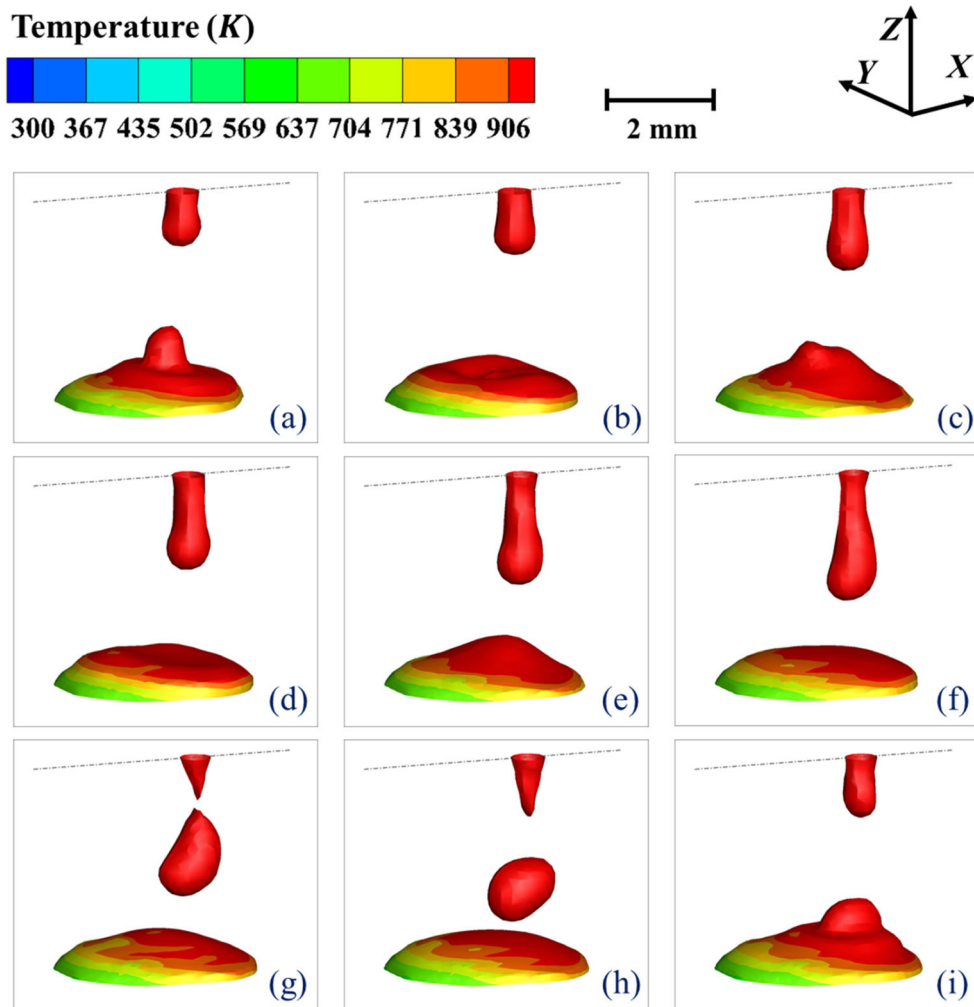
Using the operating parameters listed in Table 2, the deposition processes of SPSL, SPTL, and SPFL of 5A05 by WAAM are calculated by the developed droplet-molten pool coupled model.

### 4.1 Droplet transfer

As with GMAW, the droplet transfer model of WAAM determines the process stability and consequently the quality of deposited layer. Generally, there are three basic forms of metal transfer in the GMAW of aluminum alloy: short circuit, globular, and spray. With the increase of welding current and voltage, the transfer model of droplet changes from short circuit to globular and to spray. Figure 4 shows the simulated droplet morphology at different moments during one falling cycle; it can be seen that the liquid metal transfers from the wire tip to molten pool by the globular model, which is consistent with Ferraresi V. A.' [35] test results. According to the static force balance theory (SFBT), in the early stage of droplet formation, surface tension is dominant, which makes the droplet remain nearly spherical. As the wire continues to melt, the droplet



**Fig. 4** The evolution of droplet shape during one falling cycle: **a**  $t=0\text{ms}$ ; **b**  $t=4\text{ms}$ ; **c**  $t=8\text{ms}$ ; **d**  $t=12\text{ms}$ ; **e**  $t=16\text{ms}$ ; **f**  $t=20\text{ms}$ ; **g**  $t=24\text{ms}$ ; **h**  $t=28\text{ms}$ ; **i**  $t=32\text{ms}$



mass increases, and the droplet is elongated under the action of electromagnetic force, gravity, and plasma drag force. When the transfer time is 16ms, the necking of droplet starts. The electromagnetic force is the dominant factor in the necking of droplet for the presence of the radial component. As shown in Fig. 5, the electromagnetic force vector is pointed toward the center of the droplet approximately, that is because the radial component of electromagnetic force is much larger than the axial component. The magnitude of electromagnetic force is in the order of  $1 \times 10^6 \text{ N/m}^3$ , and along the path from the wire tip to the bottom of droplet, the magnitude of electromagnetic force gradually decreases. The detachment of droplet from the electrode occurs at  $t = 24\text{ms}$ , and then the electromagnetic force acting on the free droplet decreases due to the limited value of current flowing through the free-flying droplet [36], as shown in Fig. 5d and Fig. 5e.

To further investigate the impact of droplet on the molten pool, the velocity field of droplet falling is necessary to be analyzed. As shown in Fig. 6, the flow velocity within the droplet varies strongly during a transfer cycle. Before necking, the force hindering droplet transfer (surface tension) is greater

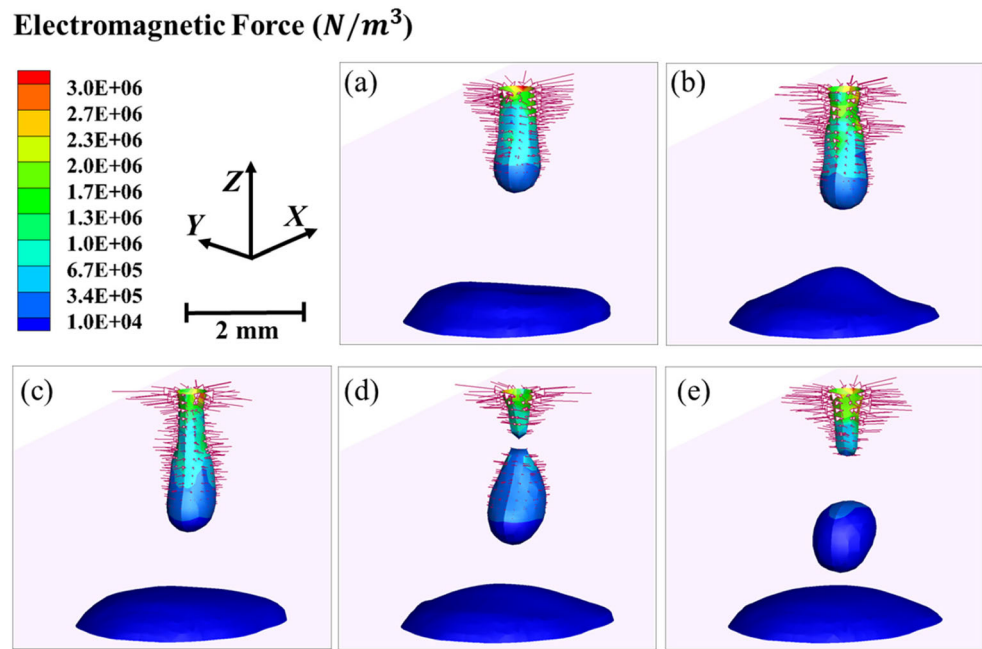
than that promoting droplet transfer (electromagnetic force, gravity, and plasma drag force); the velocity of droplet is small, about 0.3 m/s. However, after necking and till to the droplet detachment, the force promoting droplet transfer is greater than that hindering droplet transfer; the droplet is accelerated. And the maximum flow velocity within droplet reaches 0.9 m/s after droplet separation, which will have a significant effect on the fluid flow in the molten pool.

Based on the conservation of mass, the theoretical radius of droplet can be obtained by the following formula:

$$r_{td} = \sqrt[3]{\frac{3V_w R_w^2}{4f_d}} \tag{30}$$

where  $V_w$  is wire feeding speed and  $f_d$  is droplet transfer frequency. By substituting the experimental parameter ( $V_w=9 \text{ m/min}$ ,  $R_w = 0.6 \text{ mm}$ ,  $f_d = 30 \text{ Hz}$ ) into Eq. (30), the theoretical radius of droplet is estimated to be 1.105 mm. From the current numerical model, the simulated radius of free-flying droplet is estimated to be 1.114mm in Fig. 4h. And compared to the theoretical radius, the error is only 0.88%.

**Fig. 5** The distribution of electromagnetic force at different moments during a transfer cycle: **a**  $t=12\text{ms}$ ; **b**  $t=16\text{ms}$ ; **c**  $t=20\text{ms}$ ; **d**  $t=24\text{ms}$ ; **e**  $t=28\text{ms}$



## 4.2 Deposit morphology and physical field of SPSL

Figure 7 shows the deposition process of the SPSL, which is a bead-on-plate situation. As the welding torch moves, the amount of welding wire cladding increases, and the length of deposition layer is becoming longer. The region where the temperature exceeds  $906\text{K}$  is the molten pool. It can be found that in the early stage, the size of the molten pool is smaller and the height of deposition layer is higher which is

also clearly observed from the height profile along the scanning direction shown in Fig. 8. These phenomena are caused by the lower substrate temperature at the beginning and higher cooling rate of liquid metal. As the deposition process progresses, more and more droplets carrying the heat accumulate on the substrate resulting in the geometry expanding of molten pool. At the same time, the height of deposition layer decreases for the liquid metal having the sufficient time to spread, which is caused by more heat accumulation and less

**Fig. 6** The distribution of velocity at different moments during a transfer cycle: **a**  $t=12\text{ms}$ ; **b**  $t=16\text{ms}$ ; **c**  $t=20\text{ms}$ ; **d**  $t=24\text{ms}$ ; **e**  $t=28\text{ms}$

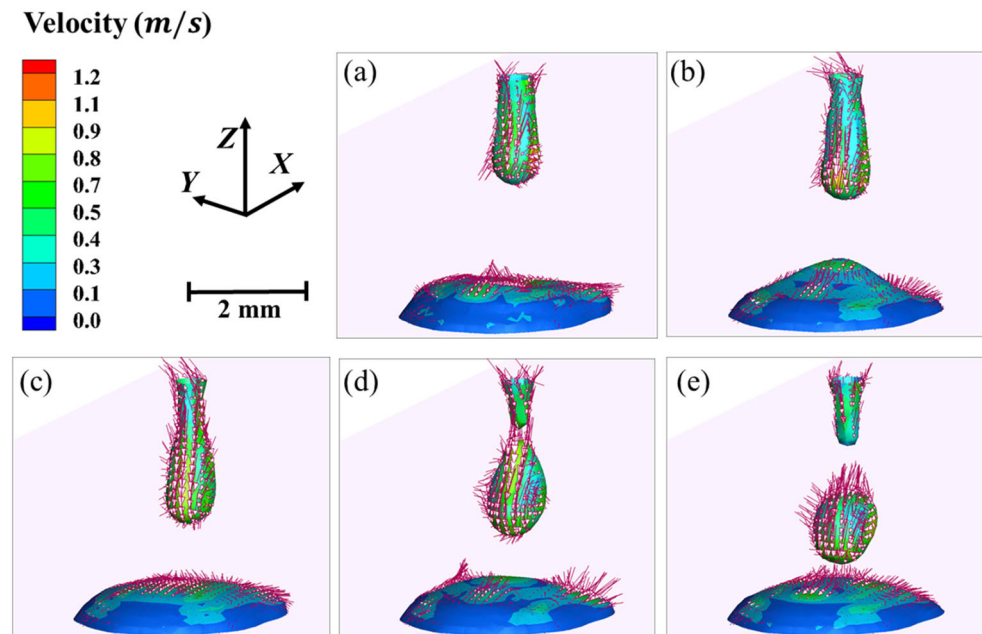
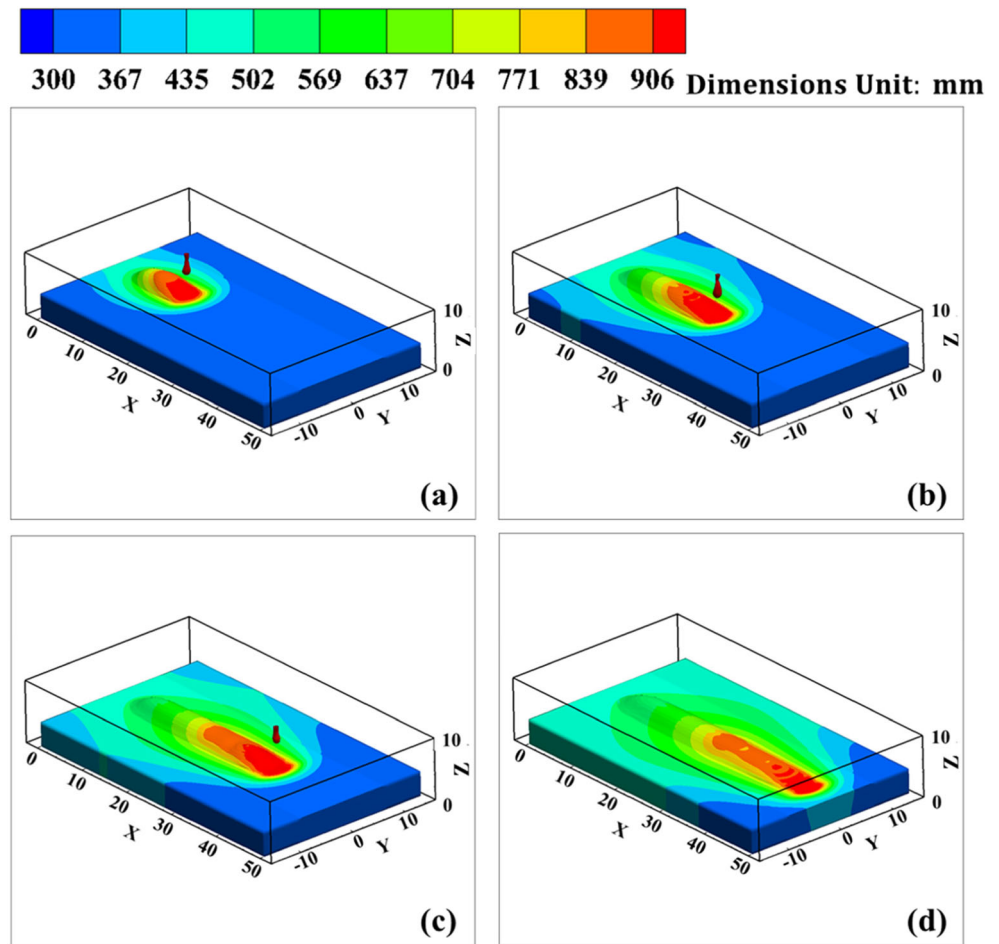


**Fig. 7** 3D views of deposit morphology of SPSL at different times: **a**  $t=0.52s$ ; **b**  $t=1.0s$ ; **c**  $t=1.52s$ ; **d**  $t=2.0s$



heat dissipation. At the moment of  $t=2.0s$ , the welding arc has been extinguished, and the molten pool gradually shrinks and will disappear completely afterwards as shown in Fig. 7d. In addition, at the location of arc-off, there is not enough metal to supplement, and the height of the end of deposition layer drops sharply, as shown in Fig. 8.

Figure 9 shows the evolution of the morphology and the corresponding temperature distribution of the deposition layer at the cross section of  $X=20mm$ . It can be seen that at the time of 0.72s, the welding torch is a little behind this cross section,

the height of deposition is closed to 0, and the molten pool has just begun to form, whose geometric size is small. At  $t=0.76s$ , the center of welding torch is exactly on the cross section, the deposition layer begins to bulge, and the dimensions of molten pool reach the maximum when the droplet carrying more energy falls into the molten pool. From the time of 0.84 to 1.04s, the welding torch has passed, and the height of deposition layer continues to increase, although the molten pool gradually shrinks. With the further loss of heat, all the liquid metal has solidified when the time is equal to 1.48s; however, the width

**Fig. 8** The height profile of SPSL along the scanning direction ( $Y=0$ )

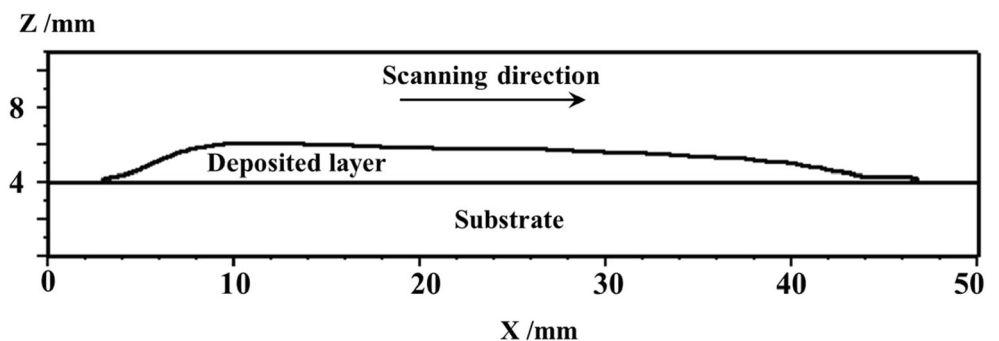
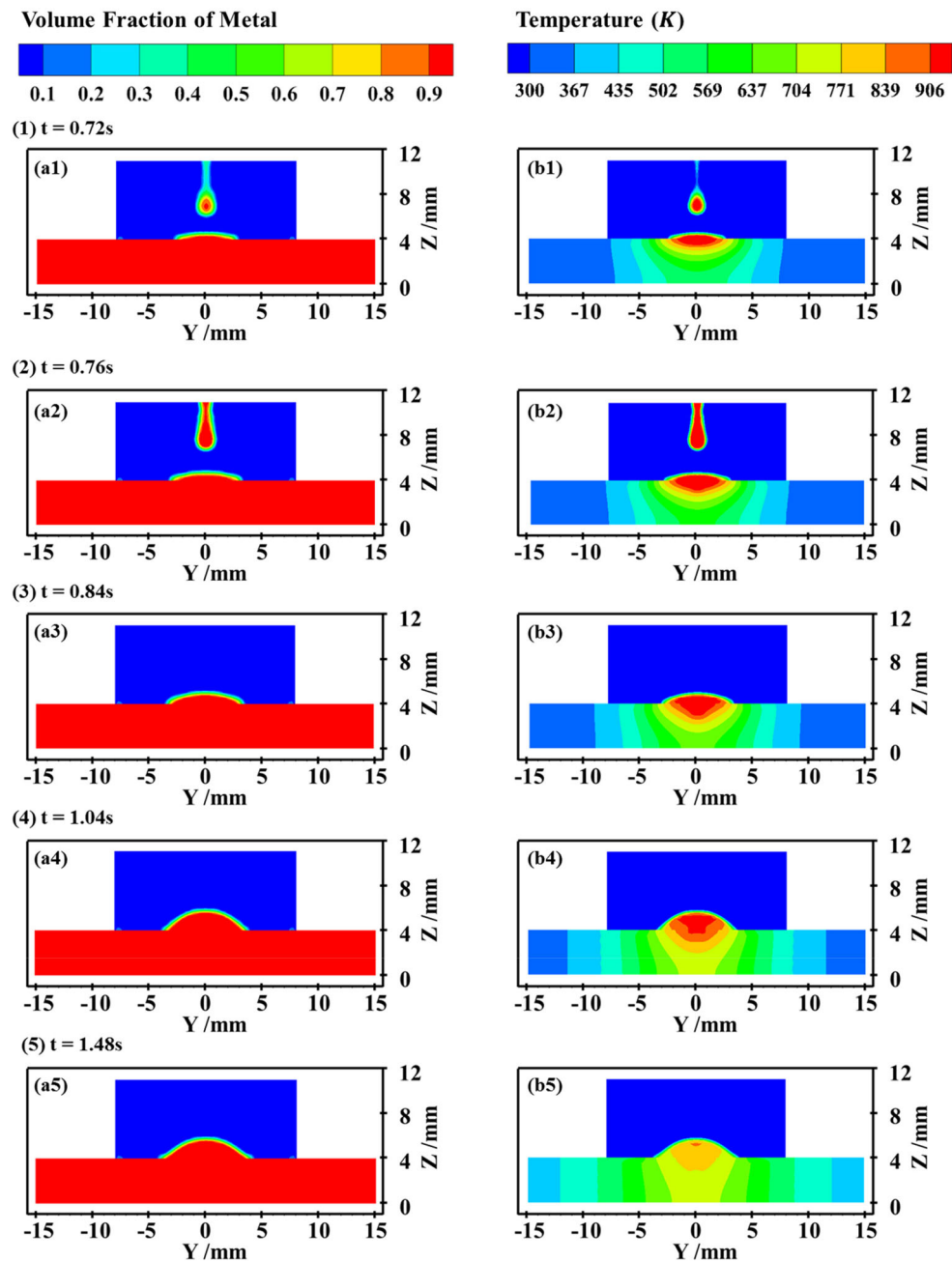


**Fig. 9** The evolution of the morphology (a1–a5) and the corresponding temperature field (b1–b5) of the deposited layer at the cross section of  $X=20\text{mm}$  over time



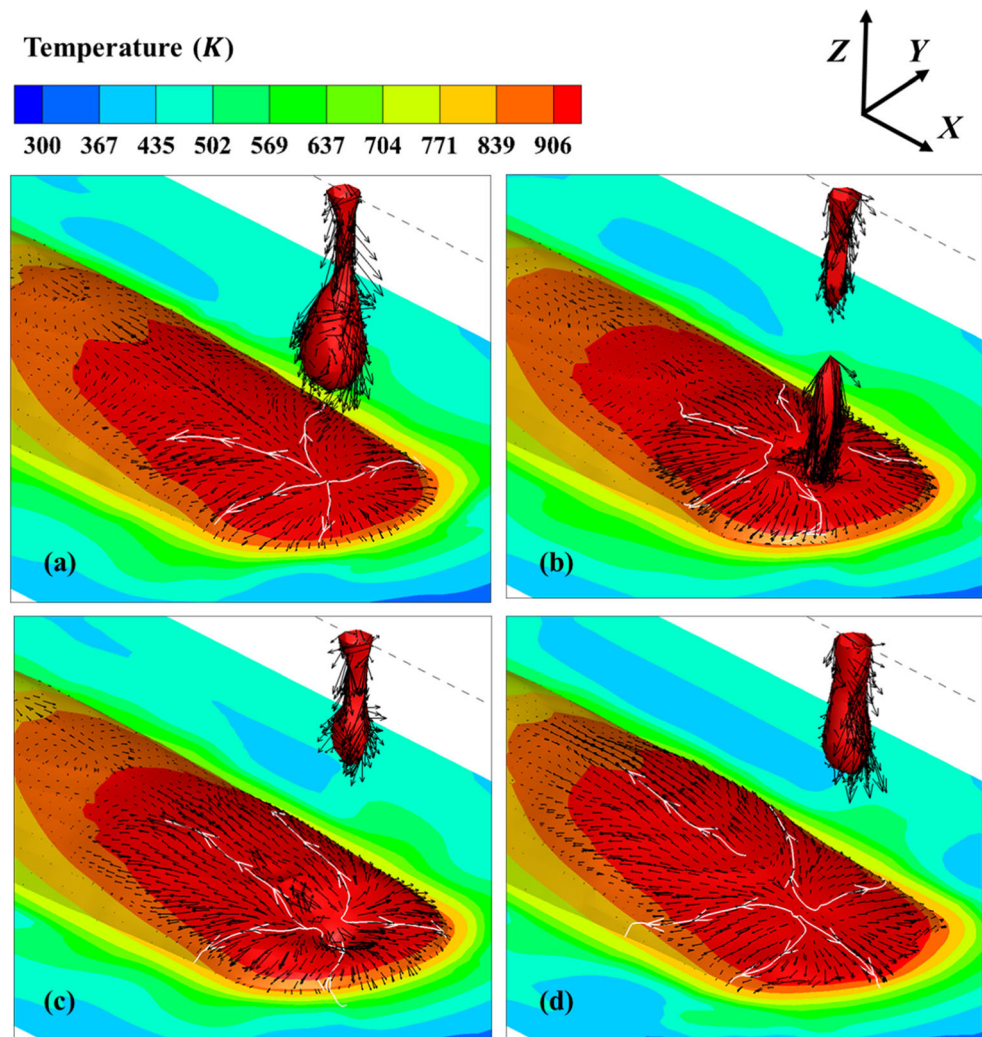
of the deposition layer has slightly expanded, which is caused by the inherent defect of enthalpy-porosity method that regards the solid as a fluid with weak momentum, and the small movement of solid can't be eliminated absolutely.

To better understand the physical mechanism of the morphology evolution of deposition layer, the temperature and fluid flow in the molten pool at different moments are analyzed. Figure 10 shows the temperature field, velocity field, and steam traces on the 3D surface of molten pool during the impingement of one droplet, which is located near  $X=21\text{mm}$ . It can be seen that the solid-liquid coexistence region of aluminum alloy is large, where the temperature ranges from 815

to 906K, and the velocity field still exists. Under the combined effect of surface tension, Marangoni force, electromagnetic force, arc pressure, gravity, and buoyancy force, the high temperature liquid metal in the center of molten pool flows to the surrounding at four moments. The behavior of the metal flowing backward promotes the continuous increase in the height of deposition layer, which is reflected in Fig. 9a3, a4, and a5. Besides the mass and heat, the momentum is also brought into the molten pool when the droplet falls, as described in Sect. 4.1. This results in that the liquid metal in the middle flows toward the bottom of molten pool, and a depressed region is formed as shown in Fig. 10b, c.



**Fig. 10** The temperature and velocity fields (the white lines are stream traces of liquid metal flow) at different moments when the weld torch is located near  $X=21\text{mm}$ : **a**  $t=0.808\text{s}$ , **b**  $t=0.820\text{s}$ , **c**  $t=0.824\text{s}$ , **d**  $t=0.832\text{s}$



Subsequently, the depressed region will vanish under the action of surface tension as shown in Fig. 10d.

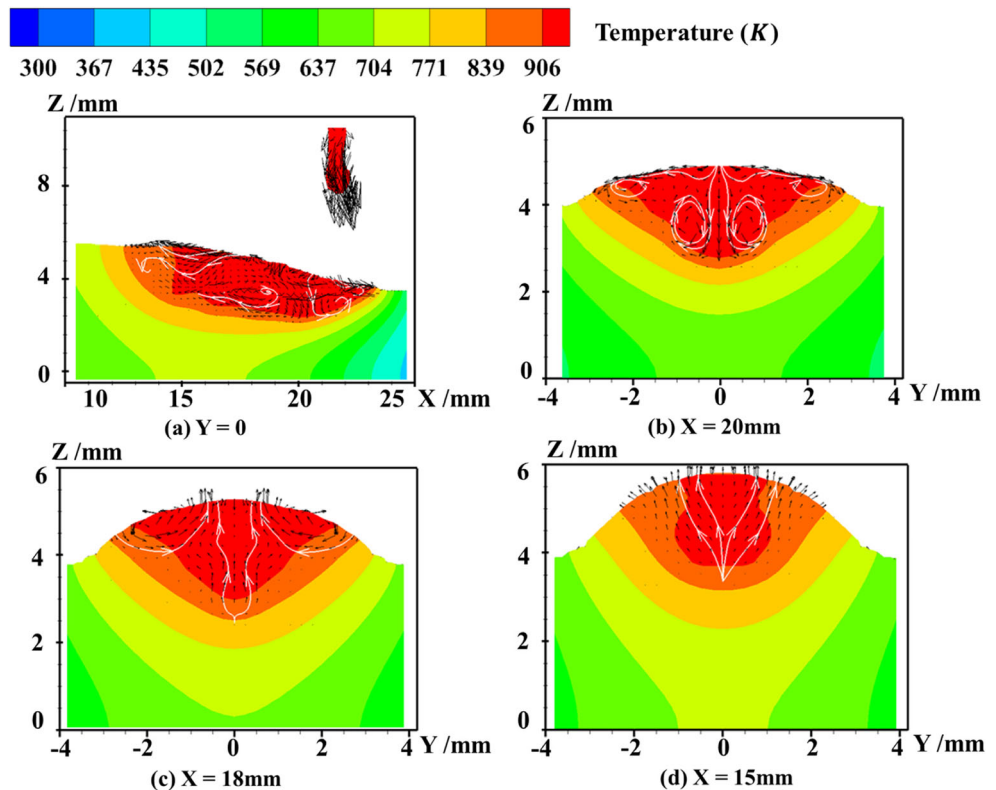
Take the longitudinal section of  $Y = 0$  and three transverse sections of  $X = 15\text{mm}$ ,  $18\text{mm}$ , and  $20\text{mm}$  from Fig. 10d to analyze the internal physical field of molten pool. As shown in Fig. 11a, the liquid metal driven and dominated by Marangoni force flows from the arc center ( $X = 21.64\text{mm}$ ) to periphery at the top of the molten pool, which results from the negative temperature coefficient of surface tension. At the bottom of molten pool, a clockwise circulation is formed. In the front of the molten pool, the temperature gradient is larger for the short distance from arc center to the liquidus boundary of molten pool. This results in a higher surface tension gradient and more severe convection compared with that of the rear of the molten pool. Comparing three cross sections shown in Fig. 11b, c, and d, it can be found that as the distance from arc center increases, the metal convection inside the molten pool weakens due to the lower temperature gradient. Analyzing Fig. 11b, a cross section only  $1.64\text{mm}$  away from arc center, the liquid metal in the middle of molten pool flows downward

and brings more heat to the bottom of molten pool under the action of gravity and electromagnetic force, causing an increase in penetration. At the cross section of  $X = 18\text{mm}$  shown in Fig. 11c, the metal flows outward on the free surface and upward inside, which will make the width of deposition wider and the reinforcement higher.

### 4.3 Deposit morphology and physical field of SPTL and SPFL

In WAAM, the path planning significantly affects the forming quality. Especially for the fabricating of thin wall part, reciprocating stacking solves the problem of hump and collapse which occur at the location of arc-on and arc-off and achieves a better forming condition compared with single direction stacking [37]. Therefore, reciprocating stacking method is adopted for the deposition of SPTL and SPFL. Meanwhile, in order to investigate the influence of interlayer idle time on the shape of deposition layer, the simulations of two extreme cases of SPTL are performed. Case 1 is the one that with

**Fig. 11** Temperature field, velocity field, and stream traces of longitudinal section and three cross sections at  $t=0.832s$ : **a** the longitudinal section of  $Y=0$ ; **b** the cross section of  $X=20mm$ ; **c** the cross section of  $X=18mm$ ; **d** the cross section of  $X=15mm$



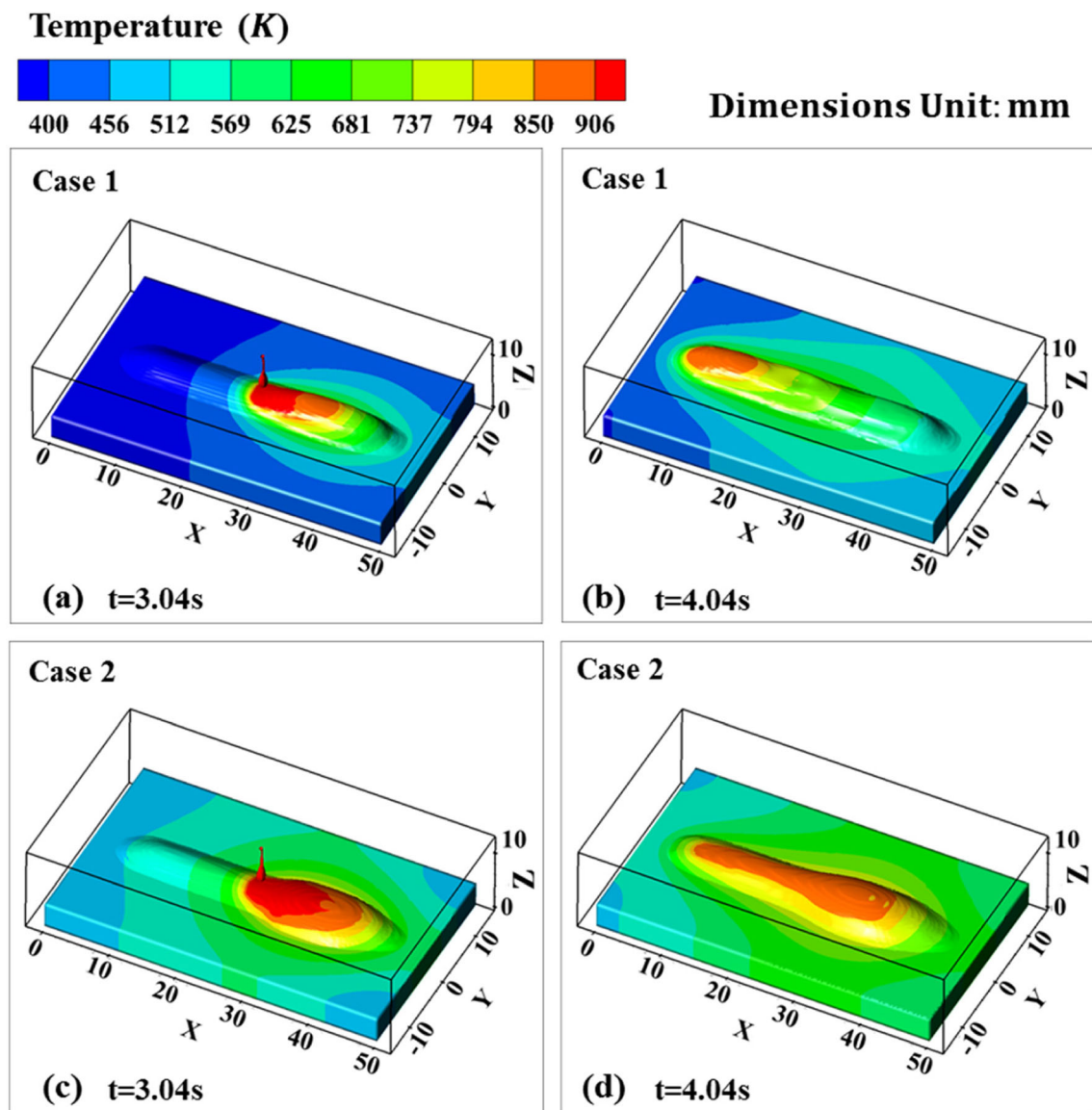
enough interlayer idle time to cool the temperature of previous layer to room temperature before the deposition of next layer, and this is directly done by resetting the temperature of whole solution domain as 300K in the current model to reduce the calculation consuming; case 2 is the one that without interlayer idle time, that is, the deposition of next layer is started immediately after the previous layer is completed.

Figure 12 shows the morphology and temperature field of 2nd deposition layer of SPTL at two moments, where a and b are the case 1 and c and d are the case 2. It can be seen at  $t=3.04s$ , and the total length of the molten pool and mushy zone of case 1 is about 10mm, which is smaller than that of case 2 about 15mm. Under the effect of heat accumulation, the average temperature of substrate and deposited layers of case 2 is more than 100 K higher than that of case 1 when the arc is just powered off, as shown in Fig. 12b and Fig. 12d. In the WAAM of thin wall, the heat conduction is the dominate way of heat dissipation, thus the cooling conditions of substrate and previous deposited layers play an important role in determining the molten pool development and fluid flow of next deposition layer. Figure 13 shows the deposited profiles of case 1 and case 2 at the location of  $X = 25mm$ ; when the depositions have been finished, it can be observed that the deposited layer of case 1 has a higher height and a narrow width. Compared with case 1, the high temperature residence time of molten pool of case 2 is longer, and the liquid metal has sufficient time to flow to periphery to widen the lateral

dimension, especially in the position of arc extinguishing and successive starting where  $X$  is from 30 to 40mm shown in Fig. 12d. Also for case 2, because of the different heat accumulation states at different positions, the dimensional unevenness of SPTL along the scanning direction is further increased, which can also be found in the experimental result of Fig. 2b.

Figure 14 shows the distributions of velocity magnitude and stream traces of case 1 and case 2 when the wire arrives at the middle of 2nd deposition layer. For both cases, the magnitudes of velocity of droplets are much greater than that of molten pool. Similar to the 1st deposition layer shown in Fig. 11a, the liquid metal on the free surface of molten pool and behind the arc flows backward, which is driven and dominated by the Marangoni force, and a clockwise circulation is also formed inside the molten pool. Due to the smaller molten pool size and higher temperature gradient, the fluid flow of case 1 under the arc is fiercer than that of case 2. And for case 2, a high-flow area occurs at the rear of molten pool under the acting of Marangoni force and gravity.

Obviously, the interlayer idle time is necessary to obtain good deposition accuracy. Therefore, the deposition of SPFL is carried out with enough interlayer cooling time. Figure 15 shows the deposit morphology of SPFL and the corresponding temperature field at the moment of 10.16s. Because the interlayer cooling time is long enough, it can be found that the substrate temperature is relatively low after the deposition is finished. The uniformity of deposit height is fairly good,



**Fig. 12** 3D views of deposit morphology and temperature field of SPFL in second layer at  $t = 3.04s$  and  $t = 4.04s$ ; **a** and **b** are case 1 that with interlayer idle time; **c** and **d** are case 2 that without interlayer idle time

especially for both ends attributed to the excessive metal of arc-on to supplement the missing metal of arc-off. Figure 16 shows the variations of the width of deposition layer (the measurement of width of  $N$ th layer is performed when  $N$  layers have been deposited) and the height of deposited layers at the cross section of  $X = 25mm$  during the forming process of SPFL; it can be seen that the height of deposited layers increases with the number of layer, but starting from the 2nd layer, the height increment is lower than the height of 1st layer, which is bead-on-plate situation, for no sufficient material support. The width of deposition layer varies fast firstly, decreasing from 7.76mm of 1st layer to 4.52mm of 4th layer, and then remains almost stable, and it could be concluded that the dimension evolution of deposition layer has reached a

relatively stable state when it comes to 4th layer for single-pass multi-layer WAAM with enough interlayer cooling time. In addition, it should be noted that the width of previous deposited layers will increase slightly as the calculation proceeds and the deposit profile would be flatter as shown in Fig. 15, which resulted from the inherent shortcoming of enthalpy-porosity method used in the current model to handle the metal melting and solidification as mentioned in Sect. 4.2.

The phenomenon of liquid metal collapse, during the deposition process of SPFL, is observed in both experiment and simulation. As shown in Fig. 17, it's the numerical results of metal collapse and correlated temperature field and fluid flow which occur at the left end of 4th layer. There are two main causes for this phenomenon, the impingement effect of droplet



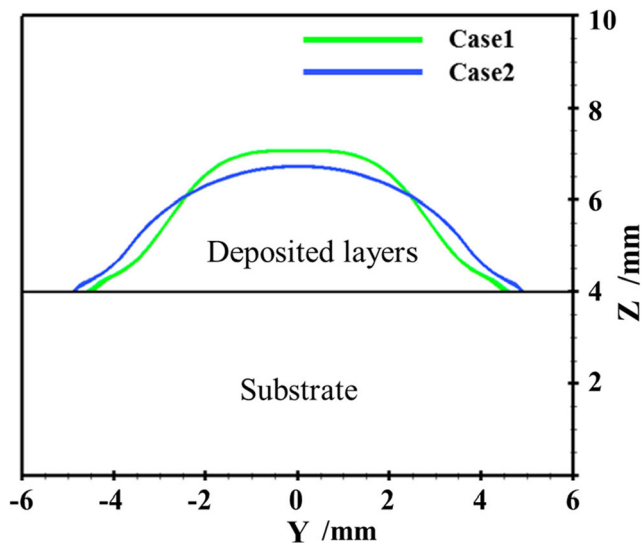


**Fig. 13** Comparison of deposit profile of SPTL between case 1 and case 2 at  $X = 25\text{mm}$

and the lack of support material. When droplet falls into molten pool, it not only carries energy to increase the local temperature of the molten pool but also carries the longitudinal momentum in the direction of gravity and transverse momentum in the direction of scanning to cause the molten metal

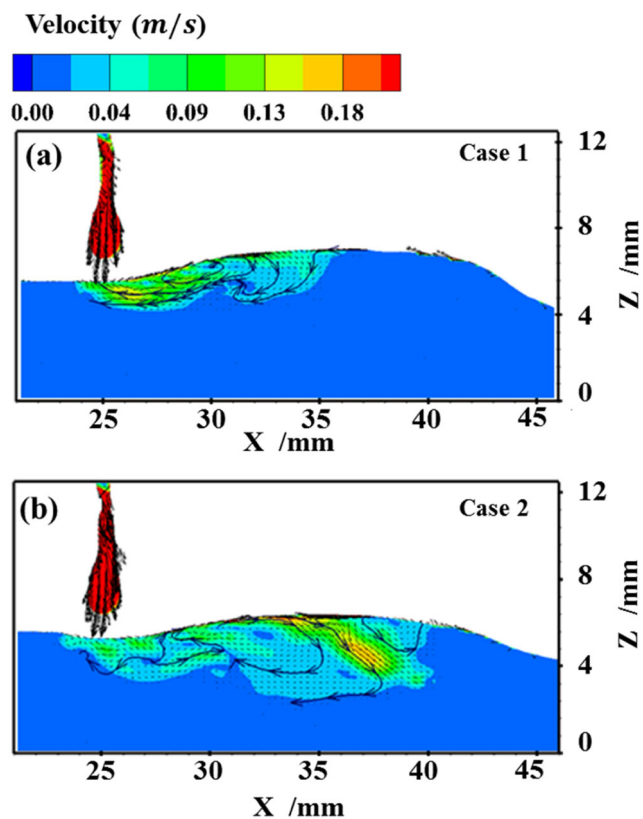


**Fig. 14** Velocity field and stream traces of case 1 (a) and case 2 (b) at  $t = 3.04\text{s}$

flowing downward and forward. Meanwhile, due to the lack of support material, the metal of molten pool will flow further to the periphery under the combined effect of Marangoni force, gravity, and surface tension, as shown in Fig. 17b, resulting in an increase of deposit length. Figure 17c shows the moment of 8.04s when the arc is just extinguished; the liquid metal still has a large velocity. Hereafter, the molten pool gradually shrinks, and the surface morphology of deposit recovers well under the action of surface tension shown in Fig. 17d.

#### 4.4 Comparisons between experimental and calculated results

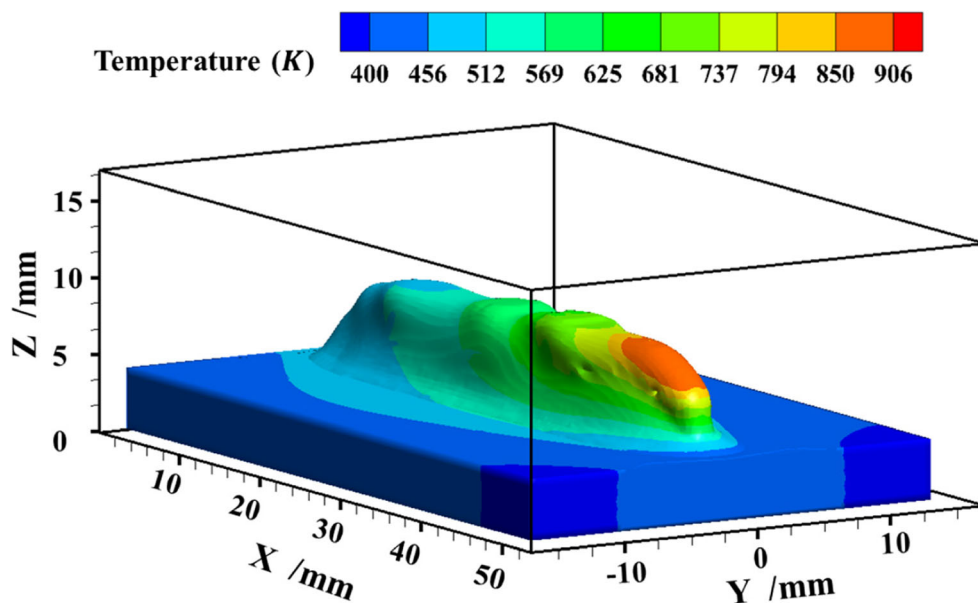
The deposit profiles calculated by the developed model are compared with those obtained by the experiments in Fig. 18a, b, c, and d corresponding to the cross-sectional planes at  $X=25\text{mm}$  of SPSL, SPTL with interlayer idle time, SPTL without interlayer idle time, and SPFL, respectively. In each picture, the simulated result of deposit profile is in the left half, and its boundary line is also extracted and reflected to the right to more intuitively compare with experimental result. In general, the simulated and experimental results are in a good agreement. Comparing Fig. 18b with c, the simulated and experimental results reflect the same changes in the deposit profile with and without interlayer idle time. Comparing Fig. 18a with d, the width difference of the 1st layer of SPFL between the simulated and experimental results becomes larger than that of SPSL; one of the reasonable explanations is that caused by the inherent shortcoming of the enthalpy-porosity method as mentioned above.

The dimensions of deposit height and length calculated by the model and measured by experiments are shown in Table 5. It can be seen that the simulated dimensions are in good agreement with those from experiments and the same trends of dimensions change among SPSL, two cases of SPTL and SPFL are found, whose maximum dimensional error does not exceed 15%. In experimental results, the deposit height of SPTL with enough interlayer idle time is increased by 90% from 1st layer to 2nd layer, while that of SPTL without interlayer idle time is only increased by 57% due to the influence of heat accumulation. The length of deposit measured by Vernier caliper is increased by 5.8% from SPSL to SPFL, which is the result of the molten metal collapse at ends of deposition layers. In the current range of calculated layers, the prediction accuracy is further enhanced with the layer number, and for SPFL, the error is only 4.3% in height and 0.5% in length of deposit.

Once the simulation parameters such as heat source dimensions are determined by a few experimental results, the present model has the ability to accurately predict the deposit morphology and physical field evolutions of WAAM process under a certain range of process parameters. Therefore, it can be



**Fig. 15** The 3D view of deposit morphology of SPFL and the related temperature distribution at  $t = 10.16s$



used to determine the appropriate heat input and interlayer cooling time to satisfy the different size control of the builds and also can be extended to the wire arc additive re-manufacturing, such as die repair, to simulate the deposition process on the complex substrate, which will be of more engineering significance.

### 5 Conclusions

In this study, a three-dimensional mathematic model has been developed to investigate the heat and metal transfer and fluid

flow in GMAW-based wire arc additive manufacturing, where the droplet formation, growth, and detachment at the end of wire electrode moving dynamically along the scanning direction are coupled to the molten pool for the first time. By the developed model, the deposition processes of SPSL, SPTL without inter-layer idle time, and SPTL and SPFL with interlayer idle time are simulated. Simultaneously, the validation of the current model is carried out by comparing the calculated deposit profiles with experimental measurements. Below are the specific findings.

- (1) The simulated results are in a good agreement with experimental measurements in the deposit profiles.

**Fig. 16** Evolution of the width of deposition layer and the height of deposited layers during the forming process of SPFL (measurements from the YOZ plane of  $X = 25mm$ )

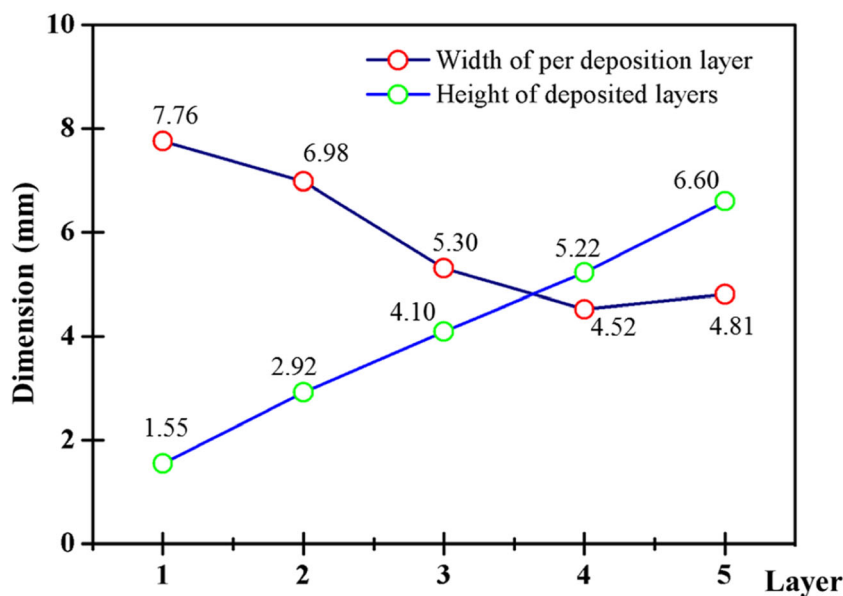


**Fig. 17** The phenomenon of metal collapse occurring before and after arc-off of 4th layer of SPFL and corresponding temperature and velocity fields: **a**  $t=7.96s$ ; **b**  $t=8.00s$ ; **c**  $t=8.04s$ ; **d**  $t=8.08s$

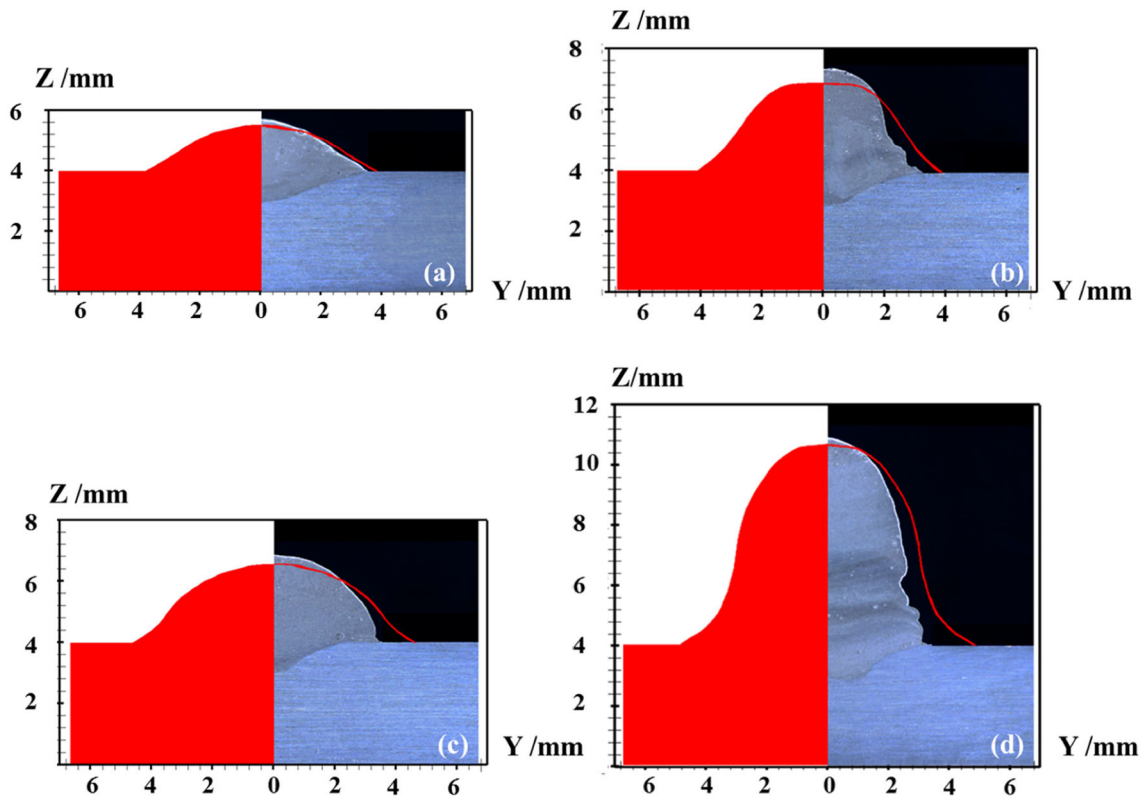
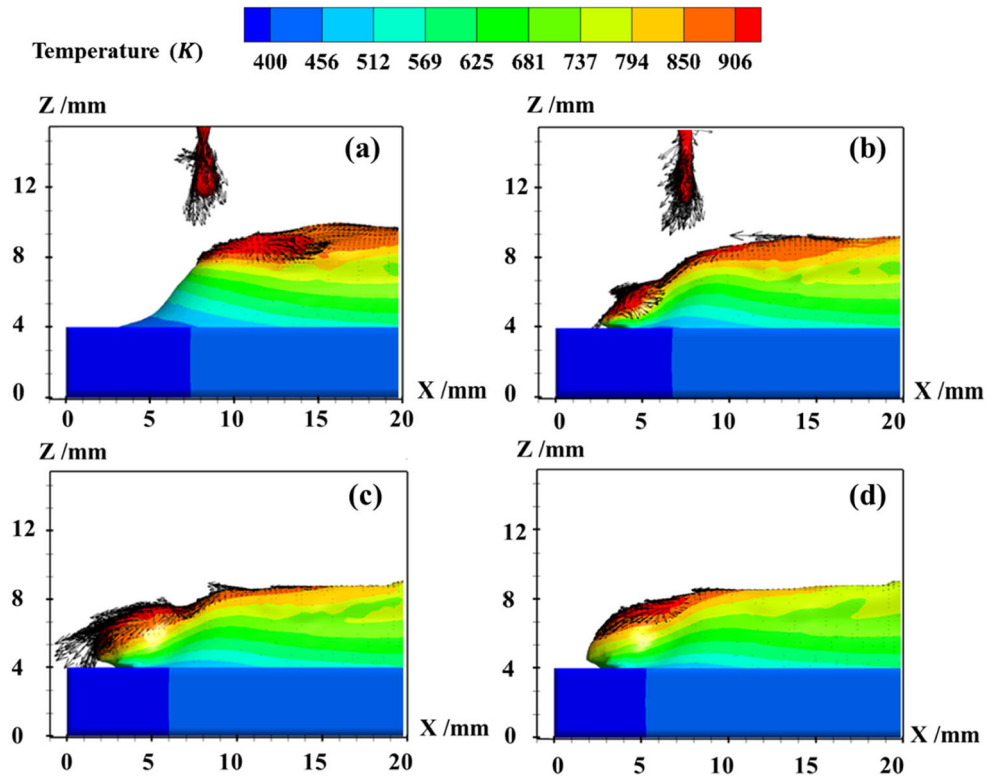


**Fig. 18** Comparisons of calculated and experimental deposits profiles at  $X=25mm$  sectional plane for: **a** SPFL; **b** case 1 of SPTL; **c** case 2 of SPTL; and **d** SPFL

**Table 5** Dimensions of the deposit height and length obtained by experimental measurements and simulations

Dimensions (mm)	SPSL		SPTL				SPFL	
			With interlayer idle time		Without interlayer idle time			
	Experiment	Simulation	Experiment	Simulation	Experiment	Simulation	Experiment	Simulation
Height of deposit ( $\lambda=25\text{mm}$ )	1.80	1.55	3.42	2.92	2.83	2.59	6.90	6.60
Length of deposit	43.28	42.47	44.12	43.08	45.03	43.93	45.80	45.57

The prediction accuracy is further enhanced with the layer number in the current range of calculated layers, and for the deposit of SPFL, its dimension error is only 4.3% in height and 0.5% in length. The significance of this work is also indicating that it is essential to couple the droplet with molten pool to accurately simulate the GMAW-based WAAM process.

- (2) Under the current operating parameters, the transfer mode of droplet is globular. After the droplet detaching from the wire electrode, the electromagnetic force within droplet becomes very small. The droplet is accelerated by gravity and plasma drag force to fall into molten pool with the maximum velocity of 0.9m/s inside, resulting in an expansion of molten pool size and a depressed region formed in the molten pool.
- (3) The liquid metal at the top of molten pool is driven and dominated by Marangoni force to flow from the center to periphery. Due to the higher temperature gradient, the metal flow at the front of the molten pool is stronger than that at the rear, and a clockwise circulation is formed at the bottom of molten pool.
- (4) The heat conduction is the dominate way of heat dissipation in the WAAM; thus the cooling conditions of previous deposited layers have a significant effect on the molten pool development and fluid flow of subsequent layers. Compared with the SPTL without interlayer idle time, SPTL with enough interlayer idle time will have a higher height and a narrow width. What's more, for the deposition of SPTL without interlayer idle time, its dimensional evenness along the scanning direction is deteriorated due to the different heat accumulation states at different positions.
- (5) Because of the impingement of droplet and the lack of support material, the height of 2nd layer decreases about 10% compared with that of 1st layer for SPFL. Simultaneously, the metal collapse occurs at the end of deposition layer in SPTL and SPFL, resulting in an increase in the length of deposit. It should be noted, however, that the increase in the length of deposit only happens in the first few layers of

WAAM of single-pass multi-layer and will remain constant afterward.

**Authors' contributions** Wenyong Zhao conducted simulations and results analysis and wrote original draft; Yanhong Wei and Renpei Liu provided innovative advices, methodology, and resource; Jinwei Long conducted experiments; Jicheng Chen provided the funding and the computing platform; Wenmin Ou revised the draft.

**Funding** This study is funded by the Priority Academic Program Development of Jiangsu Higher Education Institutions (PAPD) and China Postdoctoral Science Foundation (No. 2020M671479).

**Data availability** All data generated or analyzed during this study are included in this manuscript.

## Declarations

**Ethics approval** This research is in compliance with ethical standards. All the people involved are aware of and agree to the publication of this article.

**Consent to participate** All authors know and agree to be co-authors.

**Consent for publication** All authors agree to publish.

**Competing interests** The authors declare no competing interests.

## References

1. Gao W, Zhang Y, Ramanujan D, Ramani K, Chen Y, Williams CB, Wang CCL, Shin YC, Zhang S, Zavattieri PD (2015) The status, challenges, and future of additive manufacturing in engineering. *Comput Aided Des* 69:65–89. <https://doi.org/10.1016/j.cad.2015.04.001>
2. Rodrigues TA, Duarte V, Miranda RM, Santos TG, Oliveira JP (2019) Current status and perspectives on wire and arc additive manufacturing (WAAM). *Materials* 12(7). <https://doi.org/10.3390/ma12071121>
3. Williams SW, Martina F, Addison AC, Ding J, Pardal G, Colegrove P (2016) Wire + arc additive manufacturing. *Mater Sci Technol* 32(7):641–647. <https://doi.org/10.1179/1743284715y.0000000073>
4. Debroy T, David S (1995) Physical processes in fusion welding. *Rev Mod Phys* 67(1):85–112. <https://doi.org/10.1103/RevModPhys.67.85>

5. Ou W, Mukherjee T, Knapp GL, Wei Y, DebRoy T (2018) Fusion zone geometries, cooling rates and solidification parameters during wire arc additive manufacturing. *Int J Heat Mass Transf* 127:1084–1094. <https://doi.org/10.1016/j.ijheatmasstransfer.2018.08.111>
6. Ou W, Wei Y, Liu R, Zhao W, Cai J (2020) Determination of the control points for circle and triangle route in wire arc additive manufacturing (WAAM). *J Manuf Process* 53:84–98. <https://doi.org/10.1016/j.jmapro.2020.02.003>
7. Su C, Chen X, Gao C, Wang Y (2019) Effect of heat input on microstructure and mechanical properties of Al-Mg alloys fabricated by WAAM. *Appl Surf Sci* 486:431–440. <https://doi.org/10.1016/j.apsusc.2019.04.255>
8. Gierth M, Henckell P, Ali Y, Scholl J, Bergmann JP (2020) Wire arc additive manufacturing (WAAM) of aluminum alloy AlMg5Mn with energy-reduced gas metal arc welding (GMAW). *Materials* 13(12):2671. <https://doi.org/10.3390/ma13122671>
9. Köhler M, Hensel J, Dilger K (2020) Effects of thermal cycling on wire and arc additive manufacturing of Al-5356 components. *Metals* 10(7):952. <https://doi.org/10.3390/met10070952>
10. Oyama K, Diplas S, M'Hamdi M, Gunnæs AE, Azar AS (2019) Heat source management in wire-arc additive manufacturing process for Al-Mg and Al-Si alloys. *Additive Manufacturing* 26:180–192. <https://doi.org/10.1016/j.addma.2019.01.007>
11. Ortega AG, Galvan LC, Beaume FD, Mezrag B, Rouquette S (2017) Effect of process parameters on the quality of aluminium alloy Al5Si deposits in wire and arc additive manufacturing using a cold metal transfer process. *Taylor & Francis* 4:316–332. <https://doi.org/10.1080/10845-020-01634-6>
12. Xiong J, Zhang Y, Pi Y (2020) Control of deposition height in WAAM using visual inspection of previous and current layers. *J Intell Manuf.* <https://doi.org/10.1007/s10845-020-01634-6>
13. Vázquez L, Rodríguez N, Rodríguez I, Alberdi E, Álvarez P (2020) Influence of interpass cooling conditions on microstructure and tensile properties of Ti-6Al-4V parts manufactured by WAAM. *Welding in the World* 64(8):1377–1388. <https://doi.org/10.1007/s40194-020-00921-3>
14. Reisinger U, Sharma R, Mann S, Oster L (2020) Increasing the manufacturing efficiency of WAAM by advanced cooling strategies. *Welding in the World* 64(8):1409–1416. <https://doi.org/10.1007/s40194-020-00930-2>
15. Birmingham MJ, Nicastro L, Kent D, Chen Y, Dargusch MS (2018) Optimising the mechanical properties of Ti-6Al-4V components produced by wire + arc additive manufacturing with post-process heat treatments. *J Alloys Compd* 753:247–255. <https://doi.org/10.1016/j.jallcom.2018.04.158>
16. Cong B, Ding J, Williams S (2015) Effect of arc mode in cold metal transfer process on porosity of additively manufactured Al-6.3%Cu alloy. *Springer London* 9-12:1593–1606. <https://doi.org/10.1007/s00170-014-6346-x>
17. Zhou XZH, Wang G et al (2016) Three-dimensional numerical simulation of arc and metal transport in arc welding based additive manufacturing. *Int J Heat Mass Transf* 103:521–537. <https://doi.org/10.1016/j.ijheatmasstransfer.2016.06.084>
18. Bai XCP, Ding J et al (2018) Numerical analysis of heat transfer and fluid flow in multilayer deposition of PAW-based wire and arc additive manufacturing. *Int J Heat Mass Transf* 124(SEP):504–516. <https://doi.org/10.1016/j.ijheatmasstransfer.2018.03.085>
19. Ogino Y, Asai S, Hirata Y (2018) Numerical simulation of WAAM process by a GMAW weld pool model. *Welding in the World* 62:393–401. <https://doi.org/10.1007/s40194-018-0556-z>
20. Hejrípour F, Valentine DT, Aidun DK (2018) Study of mass transport in cold wire deposition for wire arc additive manufacturing. *Int J Heat Mass Transf* 125:471–484. <https://doi.org/10.1016/j.ijheatmasstransfer.2018.04.092>
21. Cadiou S, Courtois M, Carin M, Berckmans W, Masson PL (2020) Heat transfer, fluid flow and electromagnetic model of droplets generation and melt pool behaviour for wire arc additive manufacturing. *Int J Heat Mass Transf* 148:119102. <https://doi.org/10.1016/j.ijheatmasstransfer.2019.119102>
22. WX ZHANGJ, Tao WANG (2019) Research on forming control for single-pass multi-layer of WAAM. *TRANSACTIONS OF THE CHINA WELDING INSTITUTION* 40(12):5. <https://doi.org/10.12073/j.hjxb.2019400314>
23. Ding XLH, Yang L et al (2013) Simulation of metal transfer in GMAW based on FLUENT. *Acta Metallurgica Sinica (english Letters)* 26(3):265–270. <https://doi.org/10.1007/s40195-012-0175-4>
24. C-c L, He J-s (2017) Numerical analysis of thermal fluid transport behavior during electron beam welding of 2219 aluminum alloy plate. *Trans Nonferrous Metals Soc China* 27(6):1319–1326. [https://doi.org/10.1016/s1003-6326\(17\)60153-5](https://doi.org/10.1016/s1003-6326(17)60153-5)
25. Torrey MD, Cloutman LD, Mjolsness RC, Hirt CW (1985) NASA-VOF2D: a computer program for incompressible flows with free surfaces. *Phys Fluids* 187(7):28. <https://doi.org/10.1063/1.4931086>
26. Voller VR, Prakash C (1987) A fixed grid numerical modelling methodology for convection-diffusion mushy region phase-change problems. *Int J Heat Mass Transf* 30(8):1709–1719. [https://doi.org/10.1016/0017-9310\(87\)90317-6](https://doi.org/10.1016/0017-9310(87)90317-6)
27. Chen M, Wu CS, Lian R (2004) Numerical analysis of dynamic process of metal transfer in GMAW. *Acta Metall Sin* 40(11):1227–1232. <https://doi.org/10.1016/j.msea.2004.07.005>
28. Brackbill JU, Kothe DB, Zemach C (1992) A continuum method for modeling surface tension. *J Comput Phys* 100(2):335–354. [https://doi.org/10.1016/0021-9991\(92\)90240-Y](https://doi.org/10.1016/0021-9991(92)90240-Y)
29. S. WC (2008) *Welding thermal processes and weld pool behaviors*. China Machine Press, Beijing. ISBN: 9787111219620
30. Kumar A, DebRoy T (2003) Calculation of three-dimensional electromagnetic force field during arc welding. *J Appl Phys* 94(2):1267–1277. <https://doi.org/10.1063/1.1587006>
31. Ushio MWCS (1997) Mathematical modeling of three-dimensional heat and fluid flow in a moving gas metal arc weld pool. *Metall Mater Trans B* 28(3):509–516. <https://doi.org/10.1007/s11663-997-0118-z>
32. Zhu C, Cheon J, Tang X, Na S-J, Cui H (2018) Molten pool behaviors and their influences on welding defects in narrow gap GMAW of 5083 Al-alloy. *Int J Heat Mass Transf* 126:1206–1221. <https://doi.org/10.1016/j.ijheatmasstransfer.2018.05.132>
33. Mills CK (2002) Recommended values of thermophysical properties for selected commercial alloys || Al - LM5. 5182:32–36. <https://doi.org/10.1533/9781845690144.32>
34. Mills CK (2002) Recommended values of thermophysical properties for selected commercial alloys || Al Pure Aluminium:19–25. <https://doi.org/10.1533/9781845690144.19>
35. Hiap FVAFKMOT (2003) Metal transfer in the aluminum gas metal arc welding. doi:10.1590/S1678-58782003000300003
36. Nemchinsky V (2011) A droplet in the inter-electrode gap during gas metal arc welding. *J Phys D Appl Phys* 44(44):445203. <https://doi.org/10.1088/0022-3727/44/44/445203>
37. Nie Y, Zhang P, Wu X, Li G, Yan H, Yu Z (2018) Rapid prototyping of 4043 Al-alloy parts by cold metal transfer. *Sci Technol Weld Join* 23(6):527–535. <https://doi.org/10.1080/13621718.2018.1438236>

**Publisher's note** Springer Nature remains neutral with regard to jurisdictional claims in published maps and institutional affiliations.